Received: 11 September 2020 | Accepted: 5 December 2020

DOI: 10.1002/nbm.4465

RESEARCH ARTICLE

NMR IN BIOMEDICINE WILEY

A high-throughput imaging platform to characterize extracellular pH in organotypic three-dimensional in vitro models of liver cancer

Lynn Jeanette Savic[1,2,3] | Isabel Theresa Schobert[1,2] | Charlie Alexander Hamm[1,2,4] | Lucas Christoph Adam[1,2] | Fahmeed Hyder[1,5] | Daniel Coman[1]

[1]Department of Radiology and Biomedical Imaging, Yale University, New Haven, CT, USA

[2]Institute of Radiology, Charité—Universitätsmedizin Berlin, corporate member of Freie Universität Berlin, Humboldt-Universität, and Berlin Institute of Health, Berlin, Germany

[3]Berlin Institute of Health (BIH), Berlin, Germany

[4]Institute of Diagnostic Radiology and Neuroradiology, Greifswald University Hospital, Greifswald, Germany

[5]Department of Biomedical Engineering, Yale University, New Haven, CT, USA

Correspondence
Daniel Coman, Yale School of Medicine, Yale Cancer Center, 300 Cedar Street, TAC N144, New Haven, CT 06510, USA
Email: daniel.coman@yale.edu

Funding information
NIH, Grant/Award Number: R01 EB-023366

Given the extraordinary nature of tumor metabolism in hepatocellular carcinoma and its impact on oncologic treatment response, this study introduces a novel high-throughput extracellular pH (pH_e) mapping platform using magnetic resonance spectroscopic imaging in a three-dimensional (3D) in vitro model of liver cancer. pH_e mapping was performed using biosensor imaging of redundant deviation in shifts (BIRDS) on 9.4 T and 11.7 T MR scanners for validation purposes. 3D cultures of four liver cancer (HepG2, Huh7, SNU475, VX2) and one hepatocyte (THLE2) cell line were simultaneously analyzed (a) without treatment, (b) supplemented with 4.5 g/L D-glucose, and (c) treated with anti-glycolytic 3-bromopyruvate (6.25, 25, 50, 75, and 100 μM). The MR results were correlated with immunohistochemistry (GLUT-1, LAMP-2) and luminescence-based viability assays. Statistics included the unpaired *t*-test and ANOVA test. High-throughput pH_e imaging with BIRDS for in vitro 3D liver cancer models proved feasible. Compared with non-tumorous hepatocytes (pH_e = 7.1 ± 0.1), acidic pH_e was revealed in liver cancer (VX2, pH_e = 6.7 ± 0.1; HuH7, pH_e = 6.8 ± 0.1; HepG2, pH_e = 6.9 ± 0.1; SNU475, pH_e = 6.9 ± 0.1), in agreement with GLUT-1 upregulation. Glucose addition significantly further decreased pH_e in hyperglycolytic cell lines (VX2, HepG2, and Huh7, by 0.28, 0.06, and 0.11, respectively, all $p < 0.001$), whereas 3-bromopyruvate normalized tumor pH_e in a dose-dependent manner without affecting viability. In summary, this study introduces a non-invasive pH_e imaging platform for high-yield screening using a translational 3D liver cancer model, which may help reveal and target mechanisms of therapy resistance and inform personalized treatment of patients with hepatocellular carcinoma.

KEYWORDS
cancer therapy responses, cells and biofluids, cellular and molecular cancer imaging, hepatobiliary cancers, spectroscopic imaging

Abbreviations: 2D, two dimensional; 3-APP, 3-aminopropylphosphonate; 3-BrPA, 3-bromopyruvate; 3D, three dimensional; ATP, adenosine triphosphate;; BEGM, bronchial epithelial cell growth medium; BIRDS, biosensor imaging of redundant deviation in shifts; FBS, fetal bovine serum; FOV, field of view; GAPDH, glyceraldehyde 3-phosphate dehydrogenase; GLUT-1, glucose transporter 1; HCC, hepatocellular carcinoma; HG, HistoGel; H&E, hematoxylin/eosin; IHC, immunohistochemistry; LAMP-2, lysosome-associated membrane protein 2; MRSI, magnetic resonance spectroscopic imaging; pH_e, extracellular pH; P_i, inorganic phosphate; ROI, region of interest; SE, spin echo; SLR, Shinnar-Le Roux; SNR, signal-to-noise ratio; $TmDOTP^{5-}$, thulium (III) 1,4,7,10-tetraazacyclododecane-1,4,7,10-tetra(methylenephosphonate); TME, tumor microenvironment.

Lynn Jeanette Savic and Isabel Theresa Schobert contributed equally to this work.

1 | INTRODUCTION

Hepatocellular carcinoma (HCC) is the third most common cause of cancer-related deaths worldwide, and incidence rates continue to rise.[1] In addition to high intrinsic tumor heterogeneity due to numerous driver genes and variable mutations, HCCs are extrinsically influenced and interact with the varying components of the surrounding tumor microenvironment (TME).[2–4] A hallmark of cancer is the "Warburg effect," where glucose metabolism increases without concomitant rise in oxidative metabolism even in the presence of sufficient oxygen.[5,6]

As a consequence, large amounts of hydrogen ions and lactate generated in the intracellular milieu are extruded out into the extracellular space, acidifying the TME.[5,6] This promotes neoangiogenesis, genetic instability, metastatic development, and immune evasion of cancer cells, all of which create a favorable tumorigenic niche and contribute to poor clinical outcome.[7–10]Therefore, imaging of tumor metabolism in the TME serves as a predictive biomarker for individual susceptibility to oncological treatments. Additionally, it may enable earlier and more sensitive monitoring of tumor response to therapy that precedes morphological changes measurable with conventional anatomical imaging.[11]

pH mapping can be achieved with magnetic resonance spectroscopic imaging (MRSI) techniques using ^{1}H or ^{31}P signals.[12,13] Hyperpolarization techniques could also be employed for pH measurements using ^{13}C-labelled bicarbonate, ^{15}N-labeled pyridine derivatives, or ^{15}N-labeled imidazole.[14-16] In a recent study, hyperpolarized metabolic imaging with 1-^{13}C-pyruvate was applied to detect metabolically active HCC habitats as surrogates for residual and recurrent disease after locoregional therapy.[17] To achieve fast extracellular pH (pH_e) mapping at high resolution, we developed biosensor imaging of redundant deviation in shifts (BIRDS), which is an MRSI-based technique that directly detects paramagnetically shifted non-exchangeable signals from lanthanide Ln^{3+} complexes.[18,19] As the pH_e measurements with BIRDS rely on the chemical shift of the non-exchangeable protons and not on the peaks' amplitudes, the readout is independent of agent concentration in different tissues.[19] As opposed to many fluorescent, luminescent, or radioactive probes, MRSI provides a non-invasive approach to quantify functional cancer characteristics.[20] While BIRDS and other MRSI techniques have been tested in various experimental settings in vivo[21-24], in vitro models that mimic the TME can be beneficial alternatives that allow measurements of tumor pH_e with high throughput in human-derived cell cultures. This technique bears the potential to test the susceptibility of individual metabolic tumor phenotypes to different oncological drugs, and may help design strategies to mitigate resistance mechanisms, and thus identify a personalized targeted therapy prior to clinical application.[11,22]

Three-dimensional (3D) cell cultures have recently experienced a growing interest in cancer research and drug discovery due to their closer resemblance to the in vivo TME compared with conventional two-dimensional (2D) monolayer cell cultures.[25] Compared with cells growing in a 2D scenario, a 3D environment allows for enhanced biophysical and biochemical interactions with other cells as well as the extracellular matrix of which the 3D scaffold is made, leading to morphology and proliferation patterns that mimic in vivo tumor growth.[25–29]

The purpose of this study was to develop quantitative monitoring of tumor pH_e using BIRDS as an indicator of metabolic activity and a functional surrogate biomarker for tumor viability and therapeutic outcome in a translational in vitro 3D cell culture model for liver cancer. Hereby, this study aimed to build a high-throughput pH_e mapping platform that can be used for efficient in vitro drug testing, which may help personalize drug choice and design targeted strategies to mitigate tumor resistance mechanisms.

2 | EXPERIMENTAL

2.1 | Chemicals and reagents

Cell culture: bronchial epithelial cell growth medium (BEGM) Bullet kit; CC3170 (Lonza/Clonetics Corporation, Walkersville, MD), RPMI1640, DMEM, and MEMα (Thermo Fisher Scientific, Gibco, Waltham, MA), NaOH (GGGG), fetal bovine serum (FBS, Thermo Fisher Scientific), penicillin/streptomycin (Sigma Aldrich, St. Louis, MO), collagen I rat tail (BD Biosciences, CA, catalog no 354326). Kits: Cell Titer-Glo luminescence cell viability assay kit. Antibodies: glucose transporter 1 (GLUT-1, Thermo Fisher Scientific, catalog no PA1-46152, RRID_AB_2302087; 1:200), lysosome-associated membrane protein 2 (LAMP-2, Abcam, MA, catalog no ab13524, RRID_PAB_2134736; 1:100). Chemicals: 3-bromopyruvate (3-BrPA, Sigma Aldrich), $TmDOTP^{5-}$ (1,4,7,10-tetraazacyclododecane-1,4,7,10-tetra(methylenephosphonate)) complexed with thulium (Macrocyclics, Plano, TX), 3-aminopropylphosphonate (3-APP; Sigma Aldrich).

2.2 | Monolayer cell culture

Three well studied and characterized human hepatic cancer cell lines with varying growth characteristics were used: HepG2 (ATCC, Gaithersburg, MD; catalog no HB-8065, RRID_CVCL_0027), Huh7 (CLS Cell Lines Services, Eppelheim, Germany; catalog no 300156/p7178_HuH7, RRID_CVCL_0336), and SNU475 (ATCC; catalog no CRL-2236, RRID_CVCL_0497). Additionally, we used a human hepatocyte cell line derived from primary normal liver cells infected with SV40 large T-antigen, THLE2 (ATCC; catalog no CRL-10149, RRID_CVCL_3803), and a metastatic liver cancer cell line, VX2 (ATCC; catalog no CRL-6503, RRID_CVCL_3864), which was derived from a sarcoma of a female New Zealand White

rabbit, commonly used in a translational rabbit liver cancer model.[21,24] All experiments were performed in mycoplasma-free cells and human cell lines have been authenticated using short tandem repeat genotype profiling within three years prior to experimental use.

Cells were cultured in monolayers in RPMI 1640 (SNU, VX2), DMEM (HepG2, HuH7), and BMEM (THLE2). RPMI and DMEM were supplemented with 10% FBS, 1% penicillin-streptomycin, and 2mM L-glutamine. BEGM was supplemented according to ATCC recommendations with 2 mL bovine pituitary extract, 0.5 mL insulin, 0.5 mL hydrocortisone, 0.5 mL retinoic acid, 0.5 mL transferrin, 0.5 mL triiodothyronine, 0.5 mL hEGF and 5 ng/mL EGF, 70 ng/mL phosphoethanolamine, and 10% FBS. Cells were grown under standard cultivation conditions (37 °C, 5% CO_2) and subcultured as soon as 85% confluence was achieved. The day of seeding was defined as day 0.

2.3 | Organotypic 3D cell culture

The organotypic 3D cell culture system was based on collagen I in order to mimic a collagen-rich extracellular matrix in the fibrotic liver TME. Specifically, a collagen I solution consisting of 25 μL of 10× DMEM and 217 μL of collagen I (3.83 mg/mL) was prepared on ice. As opposed to other substances typically used to create 3D scaffolds, i.e. Matrigel, collagen is a natural protein component of the human body with collagen type I accounting for up to 90% of the organic matrix.[30] The pH_e of the solution was adjusted by dropwise addition of sodium hydroxide (Sigma Aldrich) to reach a pH of 7.0. The collagen solution was diluted using DMEM F12/GlutaMAX (Life Technologies, Carlsbad, CA) to a final concentration of 3 mg/mL. The collagen solution was kept on ice for 3 to 5 h to allow initial polymerization. A total of 65×10^3 cells were resuspended in a volume of 150 μL collagen solution. Two different well sizes (6.7 mm and 16.2 mm interior diameter) were tested. A 3D culture height of 5 mm was achieved by adding the suspension to pre-warmed small uncoated well plates (Thermo Fisher Scientific, 243,656), pre-cut into grouped wells of 10, to maximize the number of wells for simultaneous BIRDS scanning, while maintaining an appropriate sample volume for high-accuracy pH_e measurements.

The collagen-cell suspension was allowed to polymerize for 1 h at 37 °C and subsequently covered with 150 μl MEMα medium containing 1 g/L glucose. Cell cultures were allowed to grow at 37 °C, 5% CO_2 for a total of 7 d with medium exchange every 48 h (Supplementary Figure 1). On the sixth day of incubation and 24 h prior to the BIRDS scan, the paramagnetic contrast agent $TmDOTP^{5-}$ was added to the culture medium. The excess culture medium on top of the 3D cell cultures, which prevents the cultures drying out, was removed just before the BIRDS scan. However, during the 24 h of incubation, the $TmDOTP^{5-}$ agent had penetrated through the extracellular matrix of the 3D cell cultures, remaining between the cultured cells in a space similar to the tissue extracellular space, and where it provided the signal measured by BIRDS. Our previous results in animals indicate that $TmDOTP^{5-}$ can access the extracellular space but does not enter the intracellular milieu.[18] Therefore, the pH measured by BIRDS in 3D cell cultures represents exclusively the pH of the extracellular space.

To examine how increased glucose concentration affects the pH_e of different cell lines, the 3D cultures were incubated with MEMα containing 1 g/L (low glucose) and 4.5 g/L (high glucose) D-glucose, respectively, for a total incubation time of 7 d. Additionally, pH_e changes induced by the pyruvic acid analog 3-BrPA, which induces adenosine triphosphate (ATP) depletion via inhibition of the glycolytic enzyme glyceraldehyde 3-phosphate dehydrogenase (GAPDH),[31,32] were examined. On the sixth day, different concentrations of 3-BrPA (0, 6.25, 25, 50, 75, and 100 μM) were added to MEMα medium together with $TmDOTP^{5-}$, and cell cultures were incubated for another 24 h before the BIRDS scan.

2.4 | Viability assays

Cell viability testing was employed (a) to find a safe concentration range for the pH_e sensor $TmDOTP^{5-}$, and (b) to measure the effects of different glucose levels and (c) increasing concentrations of 3-BrPA on the cell lines. When the cells in the T-75 cm^2 cell culture flask reached 80-90% confluence, they were detached with trypsin-EDTA, centrifuged, suspended in medium, automatically counted (Cellometer Auto 1000, Nexcelom Bioscience, Lawrence, MA). A total of 5×10^3 cells were seeded in triplicate, covered with cell culture medium, and incubated for 72 h under steady conditions (5% CO_2, 37 °C) prior to the assay. Viability assays were performed using (a) 5, 10, 15, and 20 mM $TmDOTP^{5-}$, (b) high (4.5 g/L glucose) and low (1 g/L glucose) glucose, and (c) 6.25, 25, 50, 75, 100 μM 3-BrPA. $TmDOTP^{5-}$ and 3-BrPA were dissolved in the respective cell culture medium and added to the cell cultures for 24 h. The glucose medium was added at the time of seeding and was exchanged after 36 h using the glucose concentrations indicated above. Cell viability was measured by quantifying intracellular ATP levels using a luminescence-based kit (CellTiter-Glo, Promega, Madison, WI) following the manufacturer's protocol.

2.5 | Validation of pH_e measurements with BIRDS

The ^1H and ^{31}P MR spectra were obtained on an 11.7 T Bruker TopSpin (Billerica, MA) vertical-bore spectrometer at 300 K, using a broadband RF probe with separate coils tuned to ^1H (500.13 MHz) and ^{31}P (202.42 MHz) frequencies.

2.5.1 | Electrode-based validation

A first validation was achieved by comparing the ^{1}H BIRDS-based pH measurements with those using a pH electrode. ^{1}H BIRDS was performed using phantom samples with different pH values ranging from 6.4 to 7.7 prepared in 5 mm diameter NMR tubes (Wilmad, Vineland, NJ). Each sample contained 20 mM 3-APP and 20 mM TmDOTP^{5-} in 90% phosphate buffered saline and 10% D_2O. The pH in each of these samples was titrated by adding concentrated solutions of 1 M NaOH or 1 M HCl, and measured using a Mettler Toledo S220 pH meter (Columbus, OH). The ^{1}H MR spectra of TmDOTP^{5-} were acquired using a 7 μs square RF pulse for excitation and a 100 ms square pulse for water suppression, a spectral window of 200 kHz, a T_R of 130 ms, and 1024 averages. The MR spectra were line broadened (300 Hz) and phased (zero order) in MATLAB (Version r2018b, MathWorks, Natick, MA). The pH value in each sample was calculated from the H2, H3, and H6 proton chemical shifts of TmDOTP^{5-} as previously described.[18]

2.5.2 | ^{31}P MRS-based validation

Additionally, two ^{31}P MRS-based methods were used to validate the pH measurements with ^{1}H BIRDS. One was based on the ^{31}P chemical shift of the exogenous agent 3-APP, which is pH sensitive and has been used as a pH_e reporter.[33] The other was based on the pH dependence of the ^{31}P chemical shift from the TmDOTP^{5-} molecule itself.[34] Both 3-APP and TmDOTP^{5-} ^{31}P signals were measured relative to inorganic phosphate (P_i). The ^{31}P P_i resonance was chosen as reference for the TmDOTP^{5-} signal for two reasons. First, the culture media contains phosphate buffer, which provides a strong extracellular P_i signal that can be used together with the TmDOTP^{5-} signal for pH_e measurements. The pH sensitivity of the ^{31}P TmDOTP^{5-} signal is 14.6 ppm/pH unit, while that of the P_i signal is 1 ppm/pH unit, which is only 7% of that for TmDOTP^{5-}. Therefore, even if the P_i signal were completely intracellular, a difference of 0.4 in pH estimated between the intracellular and extracellular space would translate into an error in the chemical shift difference between the TmDOTP^{5-} and P_i signals of 0.4 ppm, which corresponds to an error of only 0.03 in the estimated pH_e. However, since the majority of the P_i signal observed in this study is extracellular, the pH_e measurement is not affected by choosing the P_i signal as a ^{31}P reference. Second, choosing P_i as a reference avoided the addition of any titrating reference (eg PCr or GPC), which could have affected the state of the cell cultures, resulting in the modification of their pH_e.

The ^{31}P MR spectra of 3-APP/TmDOTP^{5-} were acquired using a 9 μs square pulse for excitation, a spectral window of 163 kHz, a T_R of 3 s, and 200 averages. The ^{31}P MR spectra were line broadened (10 Hz) and phased (zero order) in MATLAB. For the pH calculation using the ^{31}P chemical shift difference between 3-APP and P_i ($\Delta\delta_{3\text{-APP/Pi}}$) a second-order polynomial equation was used:

$$\mathrm{pH} = a_0 + a_1 \Delta\delta_{3-\mathrm{APP/Pi}} + a_2 \Delta\delta_{3-\mathrm{APP/Pi}}{}^2 \quad (1)$$

where the coefficients a_0 = 18.639, a_1 = −0.7907, and a_2 = 0.0109 were calculated from the linear least-squares fit of pH versus $\Delta\delta_{3\text{-APP/Pi}}$. For the pH calculation using the ^{31}P chemical shift difference between TmDOTP^{5-} and P_i ($\Delta\delta_{\mathrm{TmDOTP/Pi}}$) a second-order polynomial equation was also used:

$$\mathrm{pH} = b_0 + b_1 \Delta\delta_{\mathrm{TmDOTP/Pi}} + b_2 \Delta\delta_{\mathrm{TmDOTP/Pi}}{}^2 \quad (2)$$

where the coefficients b_0 = 66.871, b_1 = 0.4250, and b_2 = 0.00074 were calculated from the linear least-squares fit of pH_e versus $\Delta\delta_{\mathrm{TmDOTP/Pi}}$. A second-order polynomial equation was used for the pH dependence of both 3-APP and TmDOTP^{5-}^{31}P signals because it provided a better fit to the experimental data than a linear equation.

2.5.3 | Reproducibility testing of MRS-based pH measurements

An additional pH validation was performed using VX2 3D cultures to confirm the consistency of the pH_e measurements with ^{1}H BIRDS. Briefly, three 5 mm NMR tubes containing 10 stacked 3D cultures in MEMα with 10% FBS, 1% penicillin/streptomycin, 20 mM TmDOTP^{5-}, and 20 mM 3-APP were prepared and the pH_e was measured using ^{1}H MRS with TmDOTP^{5-} and ^{31}P MRS with 3-APP. ^{1}H MRS showed a median pH_e of 7.38 (7.37-7.39) and ^{31}P MRS showed a median pH_e of 7.41 (7.41-7.42). Overall, these findings indicate excellent agreement between ^{1}H and ^{31}P MRSI.

2.6 | High-throughput BIRDS-based pH_e measurements in 3D cultures

2.6.1 | BIRDS in 3D cultures

Seven days after seeding (Supplementary Figure 1), the 3D cultures were subjected to pH_e mapping with BIRDS on a 9.4 T Bruker horizontal-bore spectrometer, using an elliptical ^{1}H surface transmit/receive RF coil (5 × 3.8 cm). Immediately prior to the scan, the culture medium including

$TmDOTP^{5-}$ from the top of the cell cultures was removed. T_2-weighted spin-echo (SE) images were used to locate and outline the samples in the wells. These SE images were acquired using a field of view (FOV) of 24 × 48 mm^2, a resolution of 128 × 256, with 15 slices of 0.5 mm thickness, a repetition time (T_R) of 1.5 s, and an echo time (T_E) of 15 ms. The 3D MRSI data for BIRDS was obtained using elliptical *k*-space encoding with 979 steps, an encoding gradient of 160 μs, a spectral window of 200 kHz, an FOV of 20 × 15 × 40 mm^3, a resolution of 15 × 11 × 29 to provide a voxel size of 1.3 × 1.3 × 1.3 × mm^3, a T_R of 5 ms, and 128 averages.[19] Selective excitation of $TmDOTP^{5-}$ protons was achieved using a dual-band Shinnar-Le Roux (SLR) pulse of 200 μs duration, 30 kHz width for each band, and 60 kHz separation. Water suppression was not necessary because the excitation of the water signal with this dual-band SLR pulse was less than 1%. The ^1H spectra were line broadened (300 Hz), phased (zero order) and baseline corrected (first order). The scan time was 3 min 12 s for the SE images and 9 min 18 s for pH_e mapping with BIRDS. The temperature of the wells was continuously measured and maintained at 35-37 °C during the scan by blowing hot air.

2.6.2 | MR data analysis

For BIRDS, only four or five slices contained the 3D cell cultures. When measuring the pH_e in these slices, no significant differences were detected along the vertical direction. As partial volume effects were predominantly observed at the edges of the 3D cultures, we report the pH_e only in the slice that contains the central region of the 3D cultures, where these effects are minimal. For pH_e quantification, the MRSI slices were overlaid on the SE images and a region of interest (ROI) was drawn around the well to select the voxels for analysis in MATLAB. Voxels at the margin of the well that had a partial volume larger than 50% inside the well were included in the ROI. The pH_e and temperature maps were calculated voxel by voxel based on the dependences of the H2, H3, and H6 proton chemical shifts of $TmDOTP^{5-}$ using MATLAB as previously described.[18] The pH_e and temperature determination with BIRDS depends only on $TmDOTP^{5-}$ chemical shifts, which, when expressed in ppm, are independent of the strength of the magnetic field. Both pH_e and temperature sensitivities for BIRDS with $TmDOTP^{5-}$ were found to be the same over a wide range of magnetic fields from 3 T to 11.7 T in previous studies.[18,24] However, the accuracy of BIRDS measurements depends on the signal-to-noise ratio (SNR) of the $TmDOTP^{5-}$ resonances, which is only slightly lower at low magnetic fields.[18] Because SNR also depends on several other factors (eg $TmDOTP^{5-}$ concentration, number of averages, etc), the optimal number of averages for the BIRDS experiments in this work was determined to be 128, which provided the high SNR necessary for accurate pH and temperature determination while maintaining a relatively short acquisition time (11 min).[18]

2.7 | Histological and immunohistochemical analysis

2.7.1 | HistoGel

Monolayer cultures were cultured in T-150 cm^2 flasks until confluent with an approximate number of 10 × 10^3. Cells were detached and centrifuged, and the cell pellet was resuspended in an Eppendorf tube with 10% neutral buffered formalin and left at room temperature for 60 min. Thereafter, the cells were centrifuged again, the supernatant was discarded, and the sediment remained in the tube. HistoGel (HG, Thermo Scientific, Richard-Allan Scientific, 12006679) was melted; about 0.5 mL HG was added to the tube and mixed with the sediment. HG solidified and was then dislodged from the bottom of the tube and placed in formalin in a labeled cassette.

2.7.2 | Paraffin-embedded 3D cultures

After completion of the BIRDS scan, the 3D cultures were fixated in 10% buffered formalin overnight and paraffin-embedded for histopathological correlation. The cultures were cut into 2 μm slices, deparaffinized using xylene, and rehydrated using a descending ethanol dilution series. After washing with deionized water, samples were permeabilized in boiling retrieval solution for 40 min at 95 °C. First, hematoxylin/eosin (H&E) stain was used according to standard protocols for general histopathology. Additionally, immunohistochemistry (IHC) was performed on exemplary cell untreated 3D cell culture samples. Sections were evaluated for histologic markers indicative of glycolysis (GLUT-1; dilution 1:200) and chronic acidosis (LAMP-2; dilution 1:100).

2.7.3 | ImageJ analysis

The histology samples were digitalized and visualized at up to 20× magnification using Aperio ImageScope Version 12.3 software (Leica Biosystems, Vista, CA). For quantitative comparison of GLUT-1 staining intensity among cell lines, Fiji analysis was performed.[35] Digitalized histogel

histology samples were divided into six 20X subareas per sample. Fiji software with the Trainable Weka Segmentation plugin was used for IHC membrane stain quantification.[36] Briefly, 10 cells per subarea were segmented with four different classes: the cellular membrane, cytoplasm, nucleus, and space between cells. A random forest classifier was trained with the four segmented classes and Gaussian blur, Hessian, membrane projections, Sobel filter, and difference of Gaussians as training features. The result was a classified image with binary masks of all cellular membranes in the subarea. In Fiji, the original image was converted to 8 bit gray-scale. The classified binary masks of the membranes were used for quantitative analysis of membrane stain and then redirected to the original gray-scale image. The output was mean gray values of the cellular membranes. In order to enhance the contrast of the gray intensity values to make images more intuitive to the readers, the original 0-255 scale was edited in order to achieve gray values below 10, where higher values are dark staining and low values are light staining using the following approach: $g = (220 - x)/10$, with g being the transformed and x the original gray value.

2.8 | Statistical analysis

Data from the experiments were summarized with means ± standard deviation, median, and range. Voxel-wise comparisons of data sets were evaluated using the unpaired *t*-test (two groups) or ANOVA with Tukey post hoc testing (>two groups). Statistical analysis was performed using

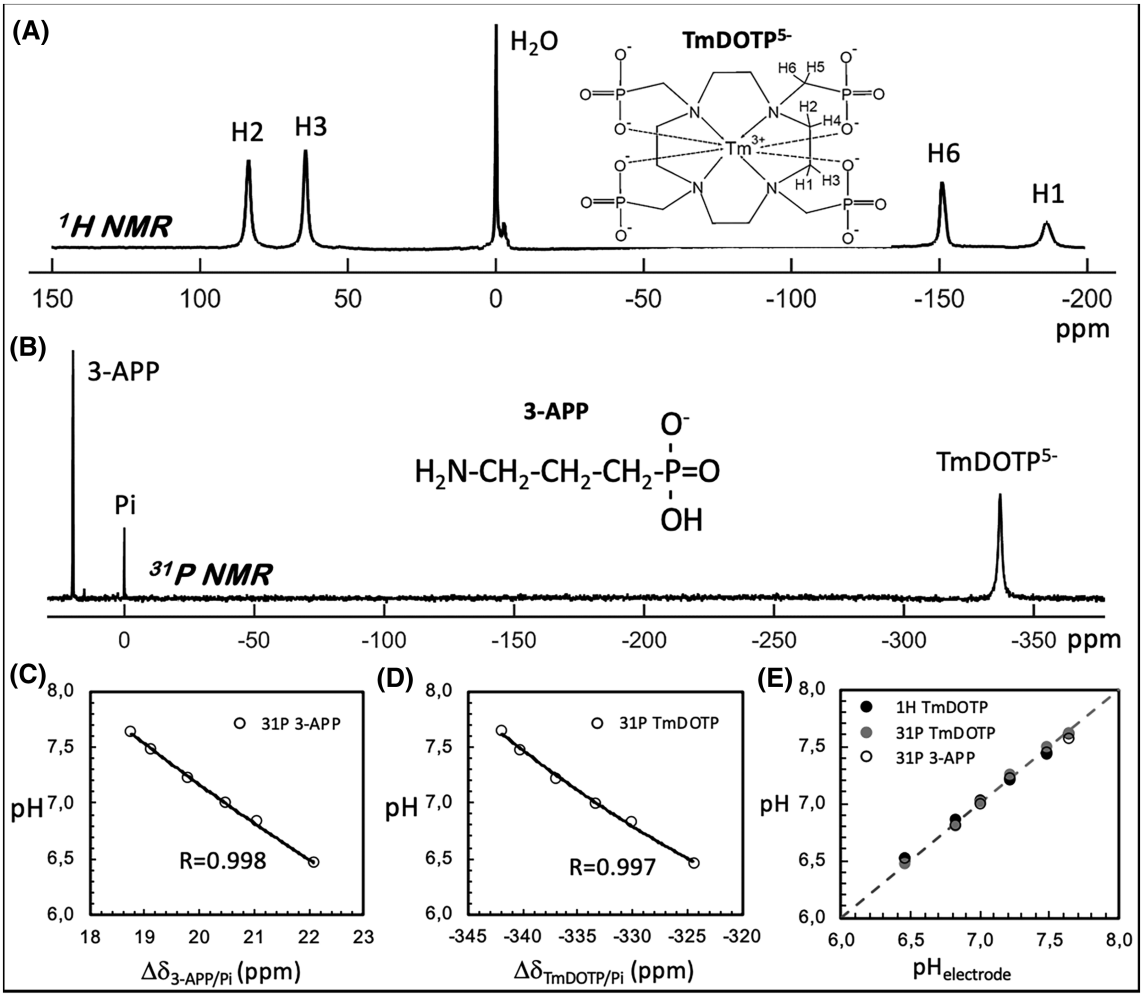

FIGURE 1 Validation of pH_e measurements with ^{1}H BIRDS using ^{31}P MRS. A, B, The pH calculation was based on ^{1}H BIRDS using the chemical shifts of H2, H3, and H6 protons of $TmDOTP^{5-}$ [18] (A), or the chemical shift difference between the ^{31}P MRS signals from 3-APP or $TmDOTP^{5-}$ and P_i (B). C, D, The ^{31}P signal from 3-APP showed a sensitivity of 2.9 ppm/pH unit (C), while the ^{31}P signal from $TmDOTP^{5-}$ showed a sensitivity of 14.6 ppm/pH unit (D). The equations that describe these two dependences (ie Equations 1 and 2) are given in Section 2. E, The MRS-based pH measurements were also compared with those obtained using the pH meter. The slopes of the pH with MRS versus pH electrode measurements were very close to unity, 0.9999 for ^{1}H with $TmDOTP^{5-}$, 0.9998 for ^{31}P with $TmDOTP^{5-}$, and 0.9976 for ^{31}P with 3-APP. To avoid excessive overlapping, these fitted lines are not shown. Instead, the identity line (gray dashed line) was used to better visualize the similarity of the pH measurements

SPSS (Version 24.0, IBM, Armonk, NY) and Prism (Version 7.0, GraphPad, San Diego, CA). A two-tailed *p*-value greater than 0.05 was considered statistically significant.

3 | RESULTS

3.1 | Validation of BIRDS-based pH_e measurements

3.1.1 | Electrode-based validation

The slopes of the linear fits of MRS-based pH versus measurements using a pH electrode were very close to unity (0.9999 for ^{1}H signals from $TmDOTP^{5-}$, 0.9998 for ^{31}P signals from $TmDOTP^{5-}$, and 0.9976 for ^{31}P signals from 3-APP), indicating an excellent agreement between all these in vitro measurements (Figure 1).

3.1.2 | ^{31}P MRSI-based validation

A second-order polynomial fit of pH versus the $\Delta\delta_{3\text{-APP/Pi}}$ difference (see Equation 1 in Section 2) provided the calibration that allowed us to calculate the pH by measuring the $\Delta\delta_{3\text{-APP/Pi}}$ difference. A similar calibration was done for the ^{31}P signal of $TmDOTP^{5-}$, where the chemical shift difference $\Delta\delta_{TmDOTP/Pi}$ was measured at different pH values and a second-order polynomial fit (see Equation 2 in Section 2) provided the calibration curve. The results showed that, at pH = 7.0, the 3-APP-based method had a sensitivity of about 2.9 ppm/pH unit, while the $TmDOTP^{5-}$ method has a five times higher sensitivity, about 14.6 ppm/pH unit (Figure 1).

3.1.3 | Reproducibility testing of MRSI-based pH measurements

Validation of pH_e measurements using ^{1}H signals from $TmDOTP^{5-}$ was also obtained in VX2 3D cultures using ^{31}P signals from 3-APP. A comparison of these measurements indicated an excellent agreement between these two MRS-based methods in all three samples investigated (Supplementary Figure 2).

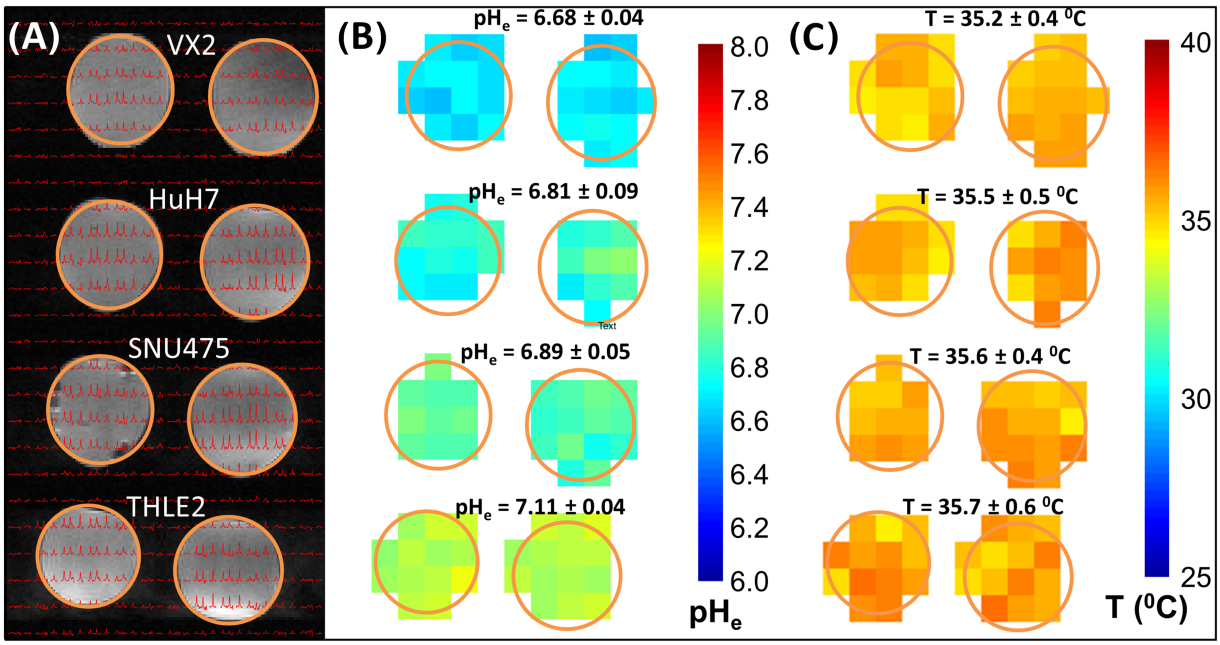

FIGURE 2 High-throughput pH_e and temperature mapping using BIRDS with $TmDOTP^{5-}$ in untreated 3D cultures. A, T_2-weighted images were used to delineate the 3D cultures within the well plate (orange). Each of VX2, HuH7, SNU475, and THLE2 cell lines were cultured in two wells in the same row. B, C, The pH_e (B) and temperature (C) in each voxel were calculated from the chemical shifts of the H2, H3, and H6 protons of $TmDOTP^{5-}$ as previously described.[18] The average pH_e and temperature, and the corresponding standard deviations for each cell line, were calculated from the voxels positioned inside the well plates containing the corresponding cell line. The results shown are obtained from a single slice in a single BIRDS experiment

3.2 | High-throughput BIRDS-based pH_e measurements in 3D cultures

3.2.1 | Comparison of different cell lines

High-throughput pH_e mapping of organotypic 3D cell cultures proved feasible. Tests with wells of two different sizes indicated that the smaller well plates (6.7 mm interior diameter) provided more stability for the scaffold and, in addition, enabled the analysis of a larger number of cell cultures simultaneously compared with the larger well plates (16.2 mm interior diameter). Therefore, the smaller well plates were used for the high-throughput pH_e-mapping experiments. A concentration of 10 mM for $TmDOTP^{5-}$ was determined to be safe for the cell cultures and provided sufficient BIRDS signal for pH_e mapping (Supplementary Figure 3). BIRDS was employed to simultaneously investigate multiple cell cultures (VX2, HepG2, HuH7, SNU475, THLE2) contained within a well plate to obtain high-throughput pH_e information (Figure 2 and Supplementary Figure 4). Multiple voxels from multiple cell culture wells were used to provide a large number of pH_e measurements for each cell type, which improved the accuracy of pH_e estimation per cell line. The temperature measurements indicate homogeneous heating using air flow of all cell culture wells (Figure 2C). pH_e mapping of untreated cells revealed a significantly lower average value for the VX2 cultures (pH_e = 6.70 ± 0.1, median 6.69, range 6.67-6.75) and HuH7 (pH_e = 6.79 ± 0.1, median 6.79, range 6.72-6.9) compared with HepG2 (pH_e = 6.82 ± 0.1, median 6.82, range 6.72-6.9) and SNU475 cultures (pH_e = 6.93 ± 0.1, median 6.93, range 6.87-6.98). As opposed to hepatic cancer cells, THLE2 hepatocytes showed physiologic liver pH_e (pH_e = 7.10 ± 0.1, median 7.1, range 7.06-7.12). Selected examples are shown in Figure 3. We also measured pH_e in negative controls containing collagen only (pH_e = 7.11 ± 0.12, median 7.1, range 6.96-7.34).

3.2.2 | Glucose supplementation effects

A significantly lower pH_e was detected in cell cultures exposed to higher glucose concentration (4.5 g/L) compared with low glucose (1 g/L) (Figure 4A and 4B). Specifically, VX2 cultures supplemented with high glucose demonstrated a pH_e decrease of 0.28 as compared with low-glucose cultures ($p < 0.001$), HepG2 cultures showed a decrease of 0.06 ($p < 0.001$), and HUH7 cultures showed a decrease of 0.11 ($p < 0.001$) (Figure 4C). Meanwhile, cell viability was not significantly affected by supplementation with 4.5 g/L glucose (Figure 4D).

3.2.3 | 3-BrPA treatment

Treatment with increasing but sub-lethal concentrations of 3-BrPA resulted in a gradual increase of pH_e in all cancer cell lines (<FIG 5>Figure 5A). An increase in 3-BrPA concentration from 6.25 to 25, 50, 7, and 100 μM resulted in an increase of pH_e for VX2 3D cultures from 7.15 ± 0.03 to 7.31 ± 0.02 ($p < 0.001$), 7.35 ± 0.02 ($p < 0.001$), 7.35 ± 0.03 ($p = 0.448$), and 7.34 ± 0.03 ($p = 0.210$), for HepG2 from 7.22 ± 0.02 to 7.31 ± 0.02 ($p < 0.001$), 7.3 ± 0.02 ($p = 0.451$), 7.38 ± 0.02 ($p < 0.001$), and 7.35 ± 0.02 ($p = 0.010$), and for HuH7 from 7.21 ± 0.04 to 7.24 ± 0.02 ($p = 0.002$),

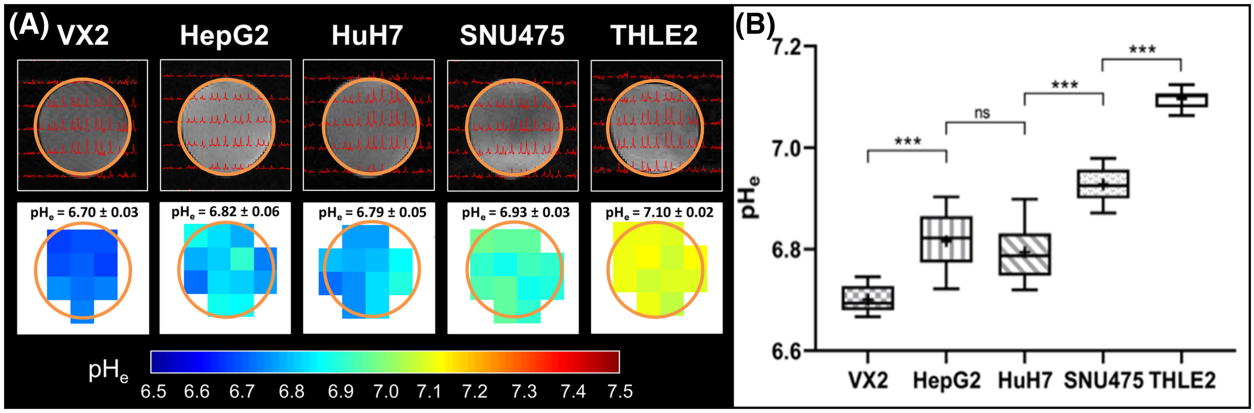

FIGURE 3 Selected examples of pH_e mapping from all five untreated 3D cultures. A, T_2-weighted images were used to delineate the 3D cultures within the well plate (orange). The top row shows the MRSI slice with the pH_e-dependent H2, H3, and H6 signal peaks of $TmDOTP^{5-}$, which were used to calculate the pH_e map in each 3D culture,[18] shown in the bottom row. The average pH_e and the standard deviation for each cell line was calculated using the voxels inside the well containing the corresponding cell line. The results shown were obtained in two separate BIRDS experiments. B, Whisker-plots illustrate the average pH_e and the statistical comparison for the five cell lines. ***$p < 0.001$; ns, not significant

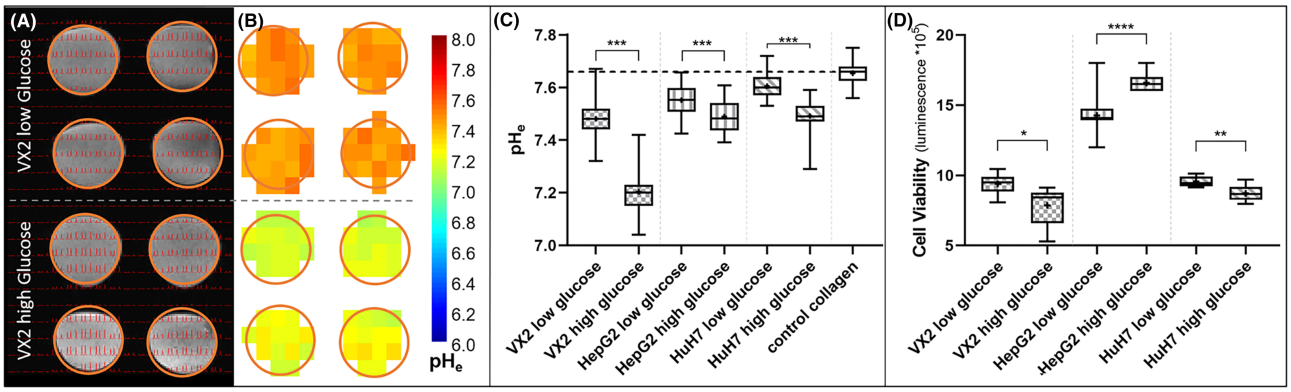

FIGURE 4 pH_e mapping with BIRDS in 3D cultures treated with high and low glucose. A, B, The MRSI dataset was overlaid on the T_2-weighted image for eight VX2 3D cultures (A), and the corresponding pH_e maps were calculated (B). The top two rows correspond to cells exposed to a culture medium with low glucose (1 g/L), while the bottom two rows were exposed to high glucose (4.5 g/L). C, BIRDS revealed a significantly lower pH_e in all cell lines treated with medium containing high glucose, compared with those exposed to low glucose. However, the pH_e of cell cultures treated with low glucose had a lower pH_e than the control with collagen only. The results shown were obtained from a single slice in a single BIRDS experiment. D, Viability assays of cells treated with high and low amounts of glucose show that cell viability was slightly higher when cells were cultured with a low amount of glucose, while only HepG2 showed more viable cells when treated with a high amount of glucose. $^*p < 0.05$, $^{**}p < 0.01$, $^{***}p < 0.001$, **** $p < 0.0001$

7.28 ± 0.02 ($p < 0.001$), 7.31 ± 0.02 ($p < 0.001$), and 7.34 ± 0.02 ($p < 0.001$), respectively (Figure 5A). The 3-BrPA doses up to 100 μM did not significantly affect cell viability (Figure 5B).

3.3 | Histologic and immunohistochemical analysis

All cancer cell lines demonstrated upregulated GLUT-1 staining intensity, which was in accordance with the pH_e findings. Specifically, VX2 showed the highest staining intensity (7.99 ± 0.38, median 8.07, range 7.26-8.31), followed by HuH7 (7.08 ± 0.53, median 6.95, range 6.48-7.81), HepG2 (6.79 ± 0.19, median 6.81, range 6.54-6.99), and SNU475 (3.94 ± 0.32, median 3.95, range 3.44-4.32), while THLE2 hepatocytes showed a very small expression of GLUT-1 (2.79 ± 0.42, median 2.81, range 2.27-3.28) (Figure 6). LAMP-2 staining was also more intense in cancer cell lines as compared with THLE2, but without measurable differences between cancer cells.

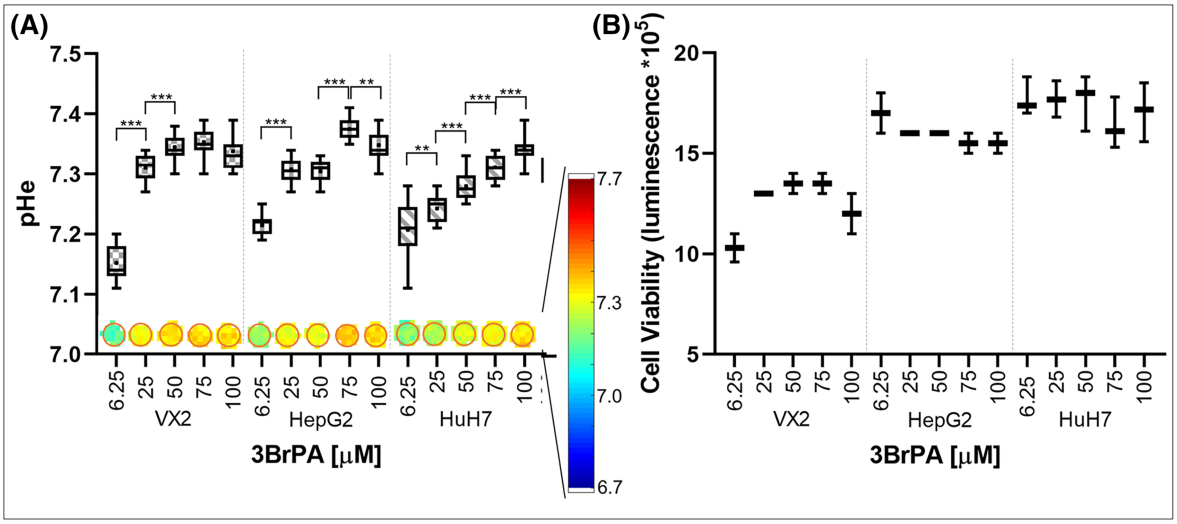

FIGURE 5 pH_e mapping with BIRDS in 3D cultures treated with 3-BrPA. A, Increasing sublethal doses (6.25, 25, 50, 75, and 100 μM) of 3-BrPA resulted in a significant increase in pH_e in all cell lines. B, Viability assays show that cell viability was not significantly impaired when cells were treated with increased 3-BrPA doses. The results shown were obtained in three separate BIRDS experiments. However, results shown for each respective cell line were obtained during the same BIRDS experiment. $^{**}p < 0.01$, $^{***}p < 0.001$

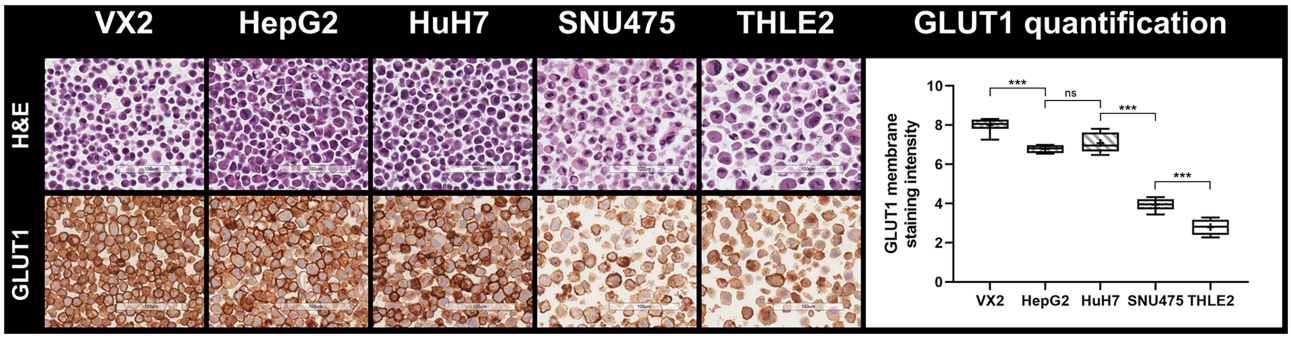

FIGURE 6 Histologic validation of pH_e measurements with GLUT-1 staining. A, H&E (top row) and GLUT-1 (bottom row) staining of all five cell lines prepared in HG are shown on the left. B, Quantitative analysis of membrane staining intensities using ImageJ showed that VX2 had the highest GLUT-1 membrane staining, significantly higher as compared with HepG2 and HuH7. However, HepG2 and HuH7 showed significantly more GLUT-1 staining compared with SNU475, which in turn had more GLUT-1 staining than the hepatocyte cell line THLE2. These histologic results are consistent with the pH_e findings (see Figure 3). ***$p < 0.001$; ns, not significant

4 | DISCUSSION

This study introduces non-invasive pH_e mapping using a translational 3D liver cancer model for high-throughput metabolic measurements in 3D organotypic in vitro models of liver cancer. These 3D models have the potential to mimic in vivo liver TMEs, where MRSI can be applied to non-invasively quantify tumor pH_e as a functional imaging biomarker for tumor viability and treatment response. In relation to a control cell line (THLE2), four liver cancer cell lines (HepG2, Huh7, SNU475, and VX2) revealed glucose-dependent tumor acidosis and pH_e neutralization upon anti-glycolytic therapy with 3-BrPA. As most liver tumors exhibit a hyperglycolytic phenotype that is associated with aggressive tumor growth and poor survival, this in vitro pH_e mapping scheme can serve as a monitoring tool to reveal mechanisms of therapy resistance and predict susceptibility and metabolic treatment response after oncologic therapies. Meanwhile, the high-throughput testing may speed-up the identification of an individualized targeted tumor therapy and ultimately facilitate the translation of in vitro findings into clinical trials and practice.[37]

While pH_e measurements using BIRDS have already been applied in vivo, this study proves the feasibility of BIRDS in 3D organotypic cell culture models of liver cancer.[21-24] 3D cell cultures allow for studying concepts of the TME in relation to drug effects on cell viability prior to clinical testing.[38] Because cancer cells cultivated in conventional 2D monolayers are generally more sensitive to anti-cancer drugs than actual tumors, drug effects are often overestimated and results from in vitro studies cannot be reproduced in vivo.[28] Several studies show that the response to drugs depends not only on the tumor type, but also on the presence and composition of the ECM, stromal cells, and immune cells.[39] In this study, collagen I, which provides a structural scaffold for cells and supports cell adhesion via integrin receptors, known to modulate tumor response to chemotherapy and radiotherapy, was used to create organotypic cell cultures.[40–42] As the majority of HCC develops in cirrhosis, the collagen-rich matrix was used to mimic the fibrillar collagen accumulation in cirrhotic livers.[43] Therefore, organotypic 3D cell cultures can serve as bridges to at least preclinical assays in vivo prior to clinical translation, with the benefits of cost-effective modeling of drug effects and toxicity with human cancer cells.[39]

Molecular imaging in the organotypic 3D culture models revealed acidic pH_e in untreated cancer cell cultures compared with physiologic liver pH_e in 3D cultures of THLE2 hepatocyte controls (pH_e = 7.1 ± 0.02). In order to capture the metabolic heterogeneity of HCC, this study included three human HCC cell lines originating from a 15-year-old Caucasian male (HepG2), a 57-year-old Asian male (HuH7), and a 43-year-old Asian male with hepatitis B (SNU475).[44–46] BIRDS revealed tumor acidosis with a pH_e of 6.82 ± 0.06 in HepG2, 6.79 ± 0.05 in HuH7, and 6.93 ± 0.03 in SNU475. Low tumoral pH_e creates a tumorigenic milieu that supports immune evasion, tumor proliferation, angiogenesis, and metastasis, all of which promote tumor progression.[9] Although of non-hepatic origin, VX2 is a well studied cell line derived from hepatic metastases with a locally invasive and metastatic growth pattern.[47] Accordingly, this study revealed the lowest pH_e to be measured in 3D cultures of VX2 cells (6.7 ± 0.03). These findings are consistent with results from previous studies that used fluorescence ratio imaging to measure a pH_e of 6.75 ± 0.06 in VX2 tumors and pH_e in physiologic liver tissue of 7.23 ± 0.08.[48] Additionally, in vivo BIRDS-based pH_e measurements in the VX2 rabbit liver tumor model performed on clinical 3 T MR scanners revealed a comparably acidic tumor pH_e (6.8 ± 0.09), while healthy liver tissue demonstrated a physiologic pH_e (7.19 ± 0.03, $p < 0.001$).[21]

Deregulated tumor metabolism is characterized by an increased glucose uptake and glycolysis rate in tumor cells, even in the presence of oxygen ("Warburg effect").[6] The subsequently increased excretion and accumulation of lactate lead to the acidification of the TME, providing a link between increased glucose uptake and microenvironmental acidification. In this study, 3D cancer cell cultures showed a significantly decreased pH_e when offered higher concentrations of glucose in the culture medium (VX2 $p < 0.001$, HepG2 $p < 0.001$, HuH7 $p < 0.001$). Accordingly,

increased expression levels of GLUT-1 were generally detectable and correlated with the pH_e, mediating an increased and facilitated cellular glucose uptake in all cancer cell lines, but not in THLE-2 hepatocytes.[49] In turn, increased glucose uptake also mirrors the metabolic activity of the cancer cells, which can be used as a surrogate marker for cell viability (eg ^{18}F-fluorodeoxyglucose positron emission tomography) and also tumor susceptibility to certain anti-cancer drugs.

In particular, there is increasing interest in the immuno-metabolic cross-talk, which comprises the competing glucose consumption of cancer and immune cells and also the inhibitory effect of low pH_e on immune cell function.[50] Besides immune-stimulating drugs, there are also targeted therapies that aim to inhibit tumor glycolysis, one of which is 3-BrPA.[51] The anti-glycolytic, and presumably anti-cancer effect of 3-BrPA is mediated by the selective pyruvylation of GAPDH and the subsequent loss of its enzymatic function. Using sequentially increasing sublethal doses of 3-BrPA, BIRDS revealed a gradual decrease of extracellular acidity, reflecting the inhibition of GAPDH activity in cancer cells.[31] In this proof-of-concept study, this series of experiments aimed to prove the sensitivity of BIRDS to detect changes induced by varying experimental conditions. Interestingly, cell lines with a more severely hyperglycolytic phenotype and more acidic pH_e at baseline (VX2 and HuH7) also revealed a higher sensitivity towards the anti-glycolytic treatment with 3-BrPA, showing a more pronounced increase of pH_e after treatment with 3-BrPA as compared with HepG2 cells. Our results further suggest that functional changes (e.g. pH_e) may be detected at lower (sublethal) doses of 3-BrPA than changes measured by state-of-the-art viability assays (Figure 5). Such early predictive swings of a biomarker are generally desirable, as they enable more possibilities for treatment optimization. Moreover, as opposed to traditional cytotoxic chemotherapies, targeted anti-glycolytic drugs may be used in an adjuvant setting to alter the state of the TME and create a less acidic, immuno-permissive niche, where traditional chemotherapeutics and novel immune-stimulating drugs work more effectively.[52]

Several approaches exist to image tumor pH, many of which utilize radionuclides or invasive probe measurements.[20,53] In contrast, BIRDS is a non-invasive MRSI approach, which selectively quantifies the pH_e that is representative of the metabolic state of the tumor and its TME.[24] While other magnetic resonance techniques are also available, such as chemical exchange saturation transfer imaging,[54–56] BIRDS has the advantage of providing absolute pH quantification based on short relaxation times (milliseconds or less) for high-speed data acquisition,[18] which is particularly important when working with cell cultures that need to be extrinsically kept at 37 °C.

In vivo pH_e imaging with ^{1}H BIRDS using $TmDOTP^{5-}$ has been validated and previously used in tumor-bearing rat brains,[22,23] and more recently in a rabbit liver tumor model.[11,24] However, this is the first study that investigates BIRDS in cell cultures. In this study, the pH_e measurements with BIRDS were validated by several other methods, including measurements using a pH electrode, but also using both 3-APP and $TmDOTP^{5-}$ with ^{31}P signals. Additionally, by using ^{31}P MRS with 3-APP, we validated the accuracy of BIRDS pH_e measurements in the 3D cell culture setting.

One limitation of this study was the spatial resolution for the MRSI voxels ($1.3 \times 1.3 \times 1.3$ mm^3). However, even at this resolution, we obtained pH_e measurements from at least 10 voxels in each well, which significantly increases our confidence in the pH_e estimation (ie by averaging pH_e values per well). Moreover, the resolution could be improved in future experiments by using a more efficient *k*-space sampling,[19] or simply longer acquisition times. Another limitation was that a new collagen-cell suspension was created for every MR session and that the baseline pH of the collagen was titrated according to standardized protocols including color-based adjustments.[32,57,58] The visual assessment of the collagen pH during the preparation may lead to pH_e variability in 3D cell cultures of different batches. However, we assumed that this potentially affects only absolute pH_e measurements, with a negligible impact on measurements of relative pH_e alterations (e.g. following treatment with 3-BrPA), where cells from the same batch with similar baseline pH were used for comparison. To demonstrate the reproducibility of the method and confirm the validity of the results, samples prepared under the same conditions were scanned at least three times. Moreover, the 3D cell culture model proposed here could be potentially improved to mimic the TME more authentically by co-culturing stromal cells, or by adding ECM molecules such as elastin or fibronectin, which could help simulate the cancer cell growth and modulate drug response.[39] Furthermore, advancing 3D culture systems by growing patient-derived tumor cells obtained from tumor biopsy or resection may allow for an even more realistic model for metabolic tumor profiling. This may help design personalized and targeted drug regimens for individual liver cancer patients and ultimately improve their clinical outcome.[44]

In conclusion, this study introduces a novel technique for the non-invasive quantification of tumor pH_e in an organotypic 3D model of liver cancer. Given the predictive value of tumor acidosis for susceptibility and response to oncological treatments, pH_e can serve as a functional biomarker to inform personalized treatment monitoring in liver cancer patients. Therefore, this BIRDS-based pH_e imaging platform for high-throughput measurements in a translational 3D model may improve validity and speed up in vitro drug-testing to mitigate resistance mechanisms and identify a targeted tumor therapy prior to clinical use.

ACKNOWLEDGEMENTS

We would like to thank the Yale Liver Center for providing the Huh7 and SNU475 cells for this study. We thank Dr Julius Chapiro (Yale University) for his scientific advice.

CONFLICTS OF INTEREST

The authors declare no conflict of interest.

FUNDING INFORMATION

This work was primarily supported by the NIH grant R01 EB-023366. Dr. Savic received grants from the Leopoldina Postdoctoral Fellowship and the Rolf W. Günther Foundation for Radiological Sciences. Dr. Savic is a participant in the BIH-Charité Junior Clinician Scientist Program funded by the Charité-Universitätsmedizin in Berlin and the Berlin Institute of Health. Dr. Schobert received support from the Biomedical Education Program (BMEP).

DATA AVAILABILITY STATEMENT

The datasets generated and analyzed during the current study are available from the corresponding author to editors and referees at submission, and to readers upon reasonable request.

ORCID

Daniel Coman https://orcid.org/0000-0002-6289-0817

REFERENCES

1. Bray F, Ferlay J, Soerjomataram I, Siegel RL, Torre LA, Jemal A. Global cancer statistics 2018: GLOBOCAN estimates of incidence and mortality worldwide for 36 cancers in 185 countries. *CA Cancer J Clin*. 2018;68(6):394-424. https://doi.org/10.3322/caac.21492
2. Roth GS, Decaens T. Liver immunotolerance and hepatocellular carcinoma: patho-physiological mechanisms and therapeutic perspectives. *Eur J Cancer*. 2017;87:101-112. https://doi.org/10.1016/j.ejca.2017.10.010
3. Forner A, Reig M, Bruix J. Hepatocellular carcinoma. *Lancet*. 2018;391(10127):1301-1314. https://doi.org/10.1016/s0140-6736(18)30010-2
4. Reina-Campos M, Moscat J, Diaz-Meco M. Metabolism shapes the tumor microenvironment. *Curr Opin Cell Biol*. 2017;48:47-53. https://doi.org/10.1016/j.ceb.2017.05.006
5. Hanahan D, Weinberg RA. Hallmarks of cancer: the next generation. *Cell*. 2011;144(5):646-674. https://doi.org/10.1016/j.cell.2011.02.013
6. Warburg O. On respiratory impairment in cancer cells. *Science*. 1956;124(3215):269-270.
7. Vegran F, Boidot R, Michiels C, Sonveaux P, Feron O. Lactate influx through the endothelial cell monocarboxylate transporter MCT1 supports an NF-kappaB/IL-8 pathway that drives tumor angiogenesis. *Cancer Res*. 2011;71(7):2550-2560. https://doi.org/10.1158/0008-5472.Can-10-2828
8. Fischer K, Hoffmann P, Voelkl S, et al. Inhibitory effect of tumor cell-derived lactic acid on human T cells. *Blood*. 2007;109(9):3812-3819. https://doi.org/10.1182/blood-2006-07-035972
9. Damaghi M, Gillies R. Phenotypic changes of acid-adapted cancer cells push them toward aggressiveness in their evolution in the tumor microenvironment. *Cell Cycle*. 2017;16(19):1739-1743. https://doi.org/10.1080/15384101.2016.1231284
10. Tomaszewski W, Sanchez-Perez L, Gajewski TF, Sampson JH. Brain tumor microenvironment and host state: implications for immunotherapy. *Clin Cancer Res*. 2019;25(14):4202-4210. https://doi.org/10.1158/1078-0432.Ccr-18-1627
11. Savic LJ, Schobert IT, Peters D, et al. Molecular imaging of extracellular tumor pH to reveal effects of locoregional therapy on liver cancer microenvironment. *Clin Cancer Res*. 2020;26(2):428-438. https://doi.org/10.1158/1078-0432.Ccr-19-1702
12. Gillies RJ, Raghunand N, Garcia-Martin ML, Gatenby RA. pH imaging. A review of pH measurement methods and applications in cancers. *IEEE Eng Med Biol Mag*. 2004;23(5):57-64. https://doi.org/10.1109/memb.2004.1360409
13. Stubbs M, Bhujwalla ZM, Tozer GM, et al. An assessment of ^{31}P MRS as a method of measuring pH in rat tumours. *NMR Biomed*. 1992;5(6):351-359. https://doi.org/10.1002/nbm.1940050606
14. Gallagher FA, Kettunen MI, Day SE, et al. Magnetic resonance imaging of pH *in vivo* using hyperpolarized ^{13}C-labelled bicarbonate. *Nature*. 2008;453(7197):940-943. https://doi.org/10.1038/nature07017
15. Jiang W, Lumata L, Chen W, et al. Hyperpolarized ^{15}N-pyridine derivatives as pH-sensitive MRI agents. *Sci Rep*. 2015;5:9104. https://doi.org/10.1038/srep09104
16. Shchepin RV, Barskiy DA, Coffey AM, et al. ^{15}N hyperpolarization of imidazole-$^{15}N_2$ for magnetic resonance pH sensing via SABRE-SHEATH. *ACS Sens*. 2016;1(6):640-644. https://doi.org/10.1021/acssensors.6b00231
17. Perkons NR, Kiefer RM, Noji MC, et al. Hyperpolarized metabolic imaging detects latent hepatocellular carcinoma domains surviving locoregional therapy. *Hepatology*. 2020;72(1):140-154. https://doi.org/10.1002/hep.30970
18. Coman D, Trubel HK, Rycyna RE, Hyder F. Brain temperature and pH measured by ^{1}H chemical shift imaging of a thulium agent. *NMR Biomed*. 2009;22(2):229-239. https://doi.org/10.1002/nbm.1312
19. Coman D, de Graaf RA, Rothman DL, Hyder F. In vivo three-dimensional molecular imaging with Biosensor Imaging of Redundant Deviation in Shifts (BIRDS) at high spatiotemporal resolution. *NMR Biomed*. 2013;26(11):1589-1595. https://doi.org/10.1002/nbm.2995
20. Anemone A, Consolino L, Arena F, Capozza M, Longo DL. Imaging tumor acidosis: a survey of the available techniques for mapping in vivo tumor pH. *Cancer Metastasis Rev*. 2019;38(1-2):25-49. https://doi.org/10.1007/s10555-019-09782-9
21. Savic LJ, Schobert IT, Peters D, et al. Molecular imaging of extracellular tumor pH to reveal effects of locoregional therapy on liver cancer microenvironment. *Clin Cancer Res*. 2019;26(2):428-438. https://doi.org/10.1158/1078-0432.Ccr-19-1702
22. Coman D, Huang Y, Rao JU, et al. Imaging the intratumoral-peritumoral extracellular pH gradient of gliomas. *NMR Biomed*. 2016;29(3):309-319. https://doi.org/10.1002/nbm.3466
23. Huang Y, Coman D, Herman P, Rao JU, Maritim S, Hyder F. Towards longitudinal mapping of extracellular pH in gliomas. *NMR Biomed*. 2016;29(10):1364-1372. https://doi.org/10.1002/nbm.3578
24. Coman D, Peters DC, Walsh JJ, et al. Extracellular pH mapping of liver cancer on a clinical 3T MRI scanner. *Magn Reson Med*. 2020;83(5):1553-1564. https://doi.org/10.1002/mrm.28035
25. Gurski LA, Petrelli NJ, Jia X, Farach-Carson MC. 3D matrices for anti-cancer drug testing and development. *Oncol Issues*. 2010;25(1):20-25. https://doi.org/10.1080/10463356.2010.11883480

26. Kim JB. Three-dimensional tissue culture models in cancer biology. *Semin Cancer Biol*. 2005;15(5):365-377. https://doi.org/10.1016/j.semcancer.2005.05.002
27. Chitcholtan K, Sykes PH, Evans JJ. The resistance of intracellular mediators to doxorubicin and cisplatin are distinct in 3D and 2D endometrial cancer. *J Transl Med*. 2012;10:38. https://doi.org/10.1186/1479-5876-10-38
28. Edmondson R, Broglie JJ, Adcock AF, Yang L. Three-dimensional cell culture systems and their applications in drug discovery and cell-based biosensors. *Assay Drug Dev Technol*. 2014;12(4):207-218. https://doi.org/10.1089/adt.2014.573
29. Langhans SA. Three-dimensional *in vitro* cell culture models in drug discovery and drug repositioning. *Front Pharmacol*. 2018;9(6). https://doi.org/10.3389/fphar.2018.00006
30. Karsdal MA, Nielsen SH, Leeming DJ, et al. The good and the bad collagens of fibrosis—their role in signaling and organ function. *Adv Drug Deliv Rev*. 2017;121:43-56. https://doi.org/10.1016/j.addr.2017.07.014
31. Ganapathy-Kanniappan S, Geschwind JF, Kunjithapatham R, et al. Glyceraldehyde-3-phosphate dehydrogenase (GAPDH) is pyruvylated during 3-bromopyruvate mediated cancer cell death. *Anticancer Res*. 2009;29(12):4909-4918.
32. Chapiro J, Sur S, Savic LJ, et al. Systemic delivery of microencapsulated 3-bromopyruvate for the therapy of pancreatic cancer. *Clin Cancer Res*. 2014;20(24):6406-6417. https://doi.org/10.1158/1078-0432.CCR-14-1271
33. Gillies RJ, Liu Z, Bhujwalla Z. 31P-MRS measurements of extracellular pH of tumors using 3-aminopropylphosphonate. *Am J Physiol*. 1994;267(1 Pt 1):C195-C203. https://doi.org/10.1152/ajpcell.1994.267.1.C195
34. Seshan V, Germann MJ, Preisig P, Malloy CR, Sherry AD, Bansal N. $TmDOTP^{5-}$ as a ^{23}Na shift reagent for the *in vivo* rat kidney. *Magn Reson Med*. 1995;34(1):25-31. https://doi.org/10.1002/mrm.1910340106
35. Schindelin J, Arganda-Carreras I, Frise E, et al. Fiji: an open-source platform for biological-image analysis. *Nat Methods*. 2012;9(7):676-682. https://doi.org/10.1038/nmeth.2019
36. Arganda-Carreras I, Kaynig V, Rueden C, et al. Trainable Weka Segmentation: a machine learning tool for microscopy pixel classification. *Bioinformatics*. 2017;33(15):2424-2426. https://doi.org/10.1093/bioinformatics/btx180
37. Jiang L, Zhao L, Bi J, et al. Glycolysis gene expression profilings screen for prognostic risk signature of hepatocellular carcinoma. *Aging*. 2019;11(23):10861-10882. https://doi.org/10.18632/aging.102489
38. Kuhlmann J. Drug research: from the idea to the product. *Int J Clin Pharmacol Ther*. 1997;35(12):541-552.
39. Stock K, Estrada MF, Vidic S, et al. Capturing tumor complexity in vitro: comparative analysis of 2D and 3D tumor models for drug discovery. *Sci Rep*. 2016;6(1):28951. https://doi.org/10.1038/srep28951
40. Yang XB, Bhatnagar RS, Li S, Oreffo RO. Biomimetic collagen scaffolds for human bone cell growth and differentiation. *Tissue Eng*. 2004;10(7/8):1148-1159. https://doi.org/10.1089/ten.2004.10.1148
41. Dickreuter E, Cordes N. The cancer cell adhesion resistome: mechanisms, targeting and translational approaches. *Biol Chem*. 2017;398(7):721-735. https://doi.org/10.1515/hsz-2016-0326
42. Holle AW, Young JL, Spatz JP. In vitro cancer cell-ECM interactions inform in vivo cancer treatment. *Adv Drug Deliv Rev*. 2016;97:270-279. https://doi.org/10.1016/j.addr.2015.10.007
43. Iredale JP, Thompson A, Henderson NC. Extracellular matrix degradation in liver fibrosis: biochemistry and regulation. *Biochim Biophys Acta Mol Basis Dis*. 2013;1832(7):876-883. https://doi.org/10.1016/j.bbadis.2012.11.002
44. Knowles BB, Aden DP, inventors. Human hepatoma derived cell line, process for preparation thereof, and uses therefor. United States, US4393133A, July 12, 1983.
45. Nakabayashi H, Taketa K, Yamane T, Miyazaki M, Miyano K, Sato J. Phenotypical stability of a human hepatoma cell line, HuH-7, in long-term culture with chemically defined medium. *GANN Jpn J Cancer Res*. 1984;75(2):151-158.
46. Park JG, Lee JH, Kang MS, et al. Characterization of cell lines established from human hepatocellular carcinoma. *Int J Cancer*. 1995;62(3):276-282. https://doi.org/10.1002/ijc.2910620308
47. Ko YH, Pedersen PL, Geschwind JF. Glucose catabolism in the rabbit VX2 tumor model for liver cancer: characterization and targeting hexokinase. *Cancer Lett*. 2001;173(1):83-91. https://doi.org/10.1016/s0304-3835(01)00667-x
48. Martin GR, Jain RK. Noninvasive measurement of interstitial pH profiles in normal and neoplastic tissue using fluorescence ratio imaging microscopy. *Cancer Res*. 1994;54(21):5670-5674.
49. Macheda ML, Rogers S, Best JD. Molecular and cellular regulation of glucose transporter (GLUT) proteins in cancer. *J Cell Physiol*. 2005;202(3):654-662. https://doi.org/10.1002/jcp.20166
50. Kaymak I, Williams KS, Cantor JR, Jones RG. Immunometabolic Interplay in the Tumor Microenvironment. *Cancer Cell*. 2020. https://doi.org/10.1016/j.ccell.2020.09.004
51. Savic LJ, Chapiro J, Duwe G, Geschwind JF. Targeting glucose metabolism in cancer: a new class of agents for loco-regional and systemic therapy of liver cancer and beyond? *Hepatic Oncol*. 2016;3(1):19-28. https://doi.org/10.2217/hep.15.36
52. Pillai SR, Damaghi M, Marunaka Y, Spugnini EP, Fais S, Gillies RJ. Causes, consequences, and therapy of tumors acidosis. *Cancer Metastasis Rev*. 2019;38(1/2):205-222. https://doi.org/10.1007/s10555-019-09792-7
53. Gillies RJ, Raghunand N, Karczmar GS, Bhujwalla ZM. MRI of the tumor microenvironment. *J Magn Reson Imaging*. 2002;16(4):430-450. https://doi.org/10.1002/jmri.10181
54. Ward KM, Aletras AH, Balaban RS. A new class of contrast agents for MRI based on proton chemical exchange dependent saturation transfer (CEST). *J Magn Reson*. 2000;143(1):79-87. https://doi.org/10.1006/jmre.1999.1956
55. Ward KM, Balaban RS. Determination of pH using water protons and chemical exchange dependent saturation transfer (CEST). *Magn Reson Med*. 2000;44(5):799-802. https://doi.org/10.1002/1522-2594(200011)44:5<799::aid-mrm18>3.0.co;2-s
56. Wu Y, Zhou IY, Igarashi T, Longo DL, Aime S, Sun PZ. A generalized ratiometric chemical exchange saturation transfer (CEST) MRI approach for mapping renal pH using iopamidol. *Magn Reson Med*. 2018;79(3):1553-1558. https://doi.org/10.1002/mrm.26817
57. Nguyen-Ngoc KV, Cheung KJ, Brenot A, et al. ECM microenvironment regulates collective migration and local dissemination in normal and malignant mammary epithelium. *Proc Natl Acad Sci U S A*. 2012;109(39):E2595-E2604. https://doi.org/10.1073/pnas.1212834109
58. Ewald AJ. Practical considerations for long-term time-lapse imaging of epithelial morphogenesis in three-dimensional organotypic cultures. *Cold Spring Harb Protoc*. 2013;2013(2):100-117. https://doi.org/10.1101/pdb.top072884

SUPPORTING INFORMATION

Additional supporting information may be found online in the Supporting Information section at the end of this article.

How to cite this article: Savic LJ, Schobert IT, Hamm CA, Adam LC, Hyder F, Coman D. A high-throughput imaging platform to characterize extracellular pH in organotypic three-dimensional in vitro models of liver cancer. *NMR in Biomedicine*. 2021;34:e4465. https://doi.org/10.1002/nbm.4465